Supporting Information

Picolinamide Iridium Catalyst Immobilized onto Aluminum-Hydride Anchor for the Selective Dehydrogenation of Neat Formic Acid

Lujain Alrais,[a] Indranil Dutta,[a] Amol Hengne,[b] Priyanka Chakraborty,[a] Edy Abou-Hamad,[c] Shibo Xi,[b] Mohammad Misbahur Rahman,[a] Jia Zhang,[d] Benjamin W. J. Chen,[d]* Jean-Marie Basset,[a,e]* and Kuo-Wei Huang [a,b]*

a Center for Renewable Energy and Storage Technologies (CREST) and Division of Physical Science and Engineering, King Abdullah University of Science and Technology
Thuwal 23955-6900, Saudi Arabia
E-mails: jeanmarie.basset@kaust.edu.sa (J.-M.B.); hkw@kaust.edu.sa (K.-W.H.)

b Institute of Sustainability for Chemicals, Energy and Environment (ISCE^2), Agency for Science, Technology and Research (A*STAR), Singapore 138634, Singapore

c Core labs, King Abdullah University of Science and Technology, Thuwal 23955-6900, Saudi Arabia

d Institute of High-Performance Computing (IHPC), Agency for Science, Technology and Research (A*STAR), Fusionopolis Way, #16–16 Connexis, Singapore 138632, Singapore- E-mail : benjamin_chen@ihpc.a-star.edu.sg

e Ecole National Supérieure de Chimie de Paris (ENSCP), 75231 Cedex 05 Paris, France

Table of Contents

1. Experimental Procedures

General Information: All experiments were conducted by using standard Schlenk and glovebox techniques under an inert (Ar and N_2) atmosphere. The syntheses and the respective treatments of the surface species were performed using high-vacuum lines (10^{-5} mbar) and glovebox techniques. Dry solvents were distilled from a Na/K alloy under N_2 degassed using freeze pump thaw cycles. In the catalytic test, neat formic acid (99-100%) was used unless otherwise stated.

1.1 Synthesis of the Homogeneous Ir-Complex:

Complex **1** was prepared following the procedure shown in Scheme S1. In a glovebox, dry methanol (15.0 mL) was added to a mixture of pentamethylcyclopentadienyliridium(III) chloride dimer (0.60 g, 0.75 mmol) and N-(2-aminoethyl)-4-(dimethylamino)picolinimidic acid (L) (0.314 g, 1.5 mmol) in a reaction flask and stirred overnight at room temperature. Methanol was then removed in vacuo. Column chromatography was used to purify the complex using CH_2Cl_2/MeOH (50:1−20:1) as the eluent. Yield: 0.68 g, 74%. A single crystal of complex **1'** was obtained after an anion exchange of **1** with KPF_6 from a mixture of DCM and ether. ^{1}H NMR (400 MHz, D_2O): δ 8.17 (d, J = 6.8 Hz, 1H), 7.06 (d, J = 3.1 Hz, 1H), 6.79 (dd, J = 6.8, 3.1 Hz, 1H), 4.11 (s, 2H), 3.27 (t, J = 5.6 Hz, 2H), 3.11 (s, 6H), 1.61 (s, 15H), 1.45 (br);^{13}C NMR (100 MHz, D_2O): δ 173.83, 155.33, 151.31, 148.85, 110.00, 107.58, 87.11, 57.40, 45.75, 39.43, 38.69, 16.77, 7.99.

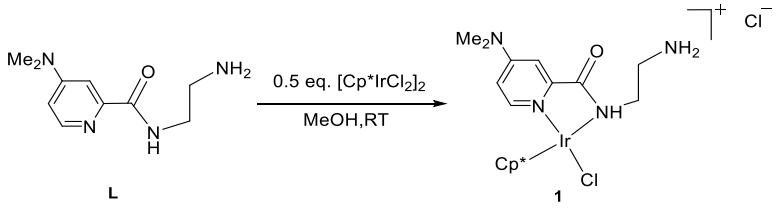

Scheme S1. Synthesis of Complex **1**

1.2 Characterizations of Complex 1

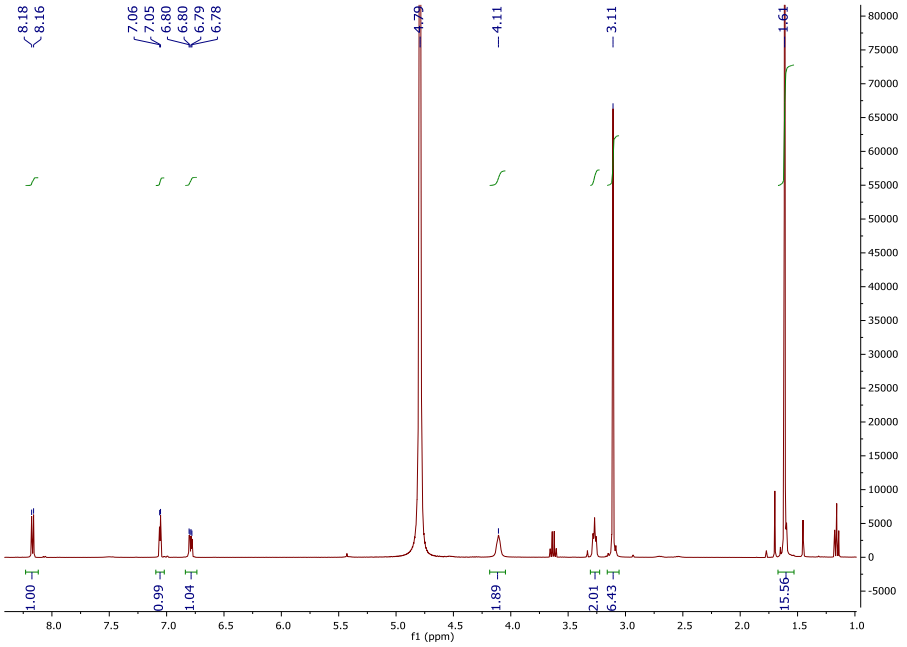

Figure S1. ^{1}H NMR spectrum of the homogeneous complex **1**

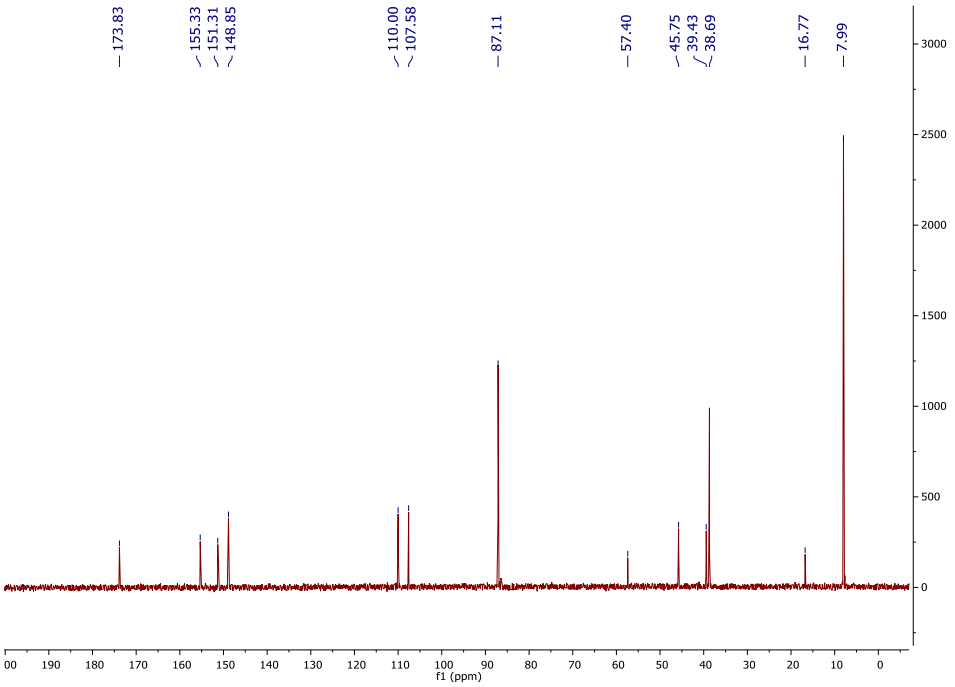

Figure S2. ^{13}C NMR spectrum of the homogeneous complex **1**

The FT-IR spectrum of complex **1** is shown in Figure S3. The characteristic bands at 3150-2830 cm^{-1} and 1350-1235 cm^{-1} belong to the stretching and bending vibration of C-H, respectively, which constitute the framework structure of the complex **1**. The broad peak at 3530 cm^{-1} was attributed to the bending vibration of N-H. The two overlapping sharp bands at 1605 and 1533 cm^{-1} can be ascribed to the typical vibrations N=C/C=C. the peaks appeared at ~1740 cm^{-1}, derived from the stretching vibration of O=C-N.

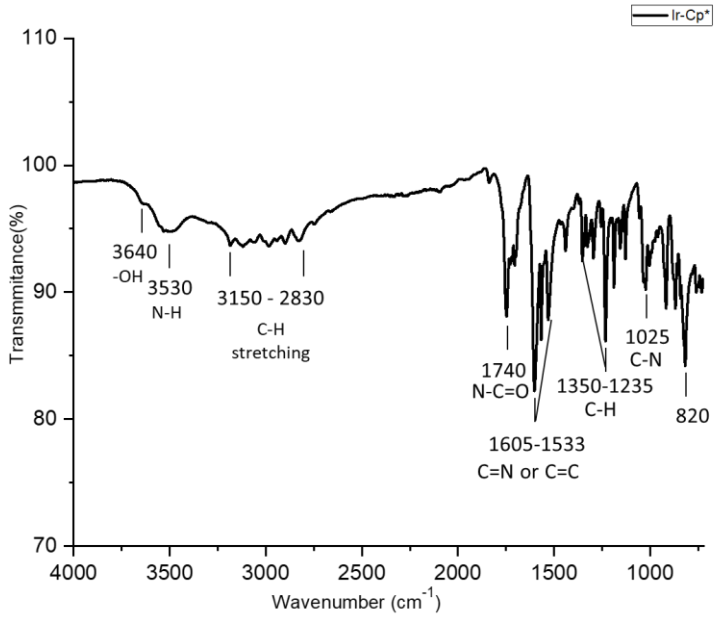

Figure S3. The IR spectrum of the homogeneous complex **1**

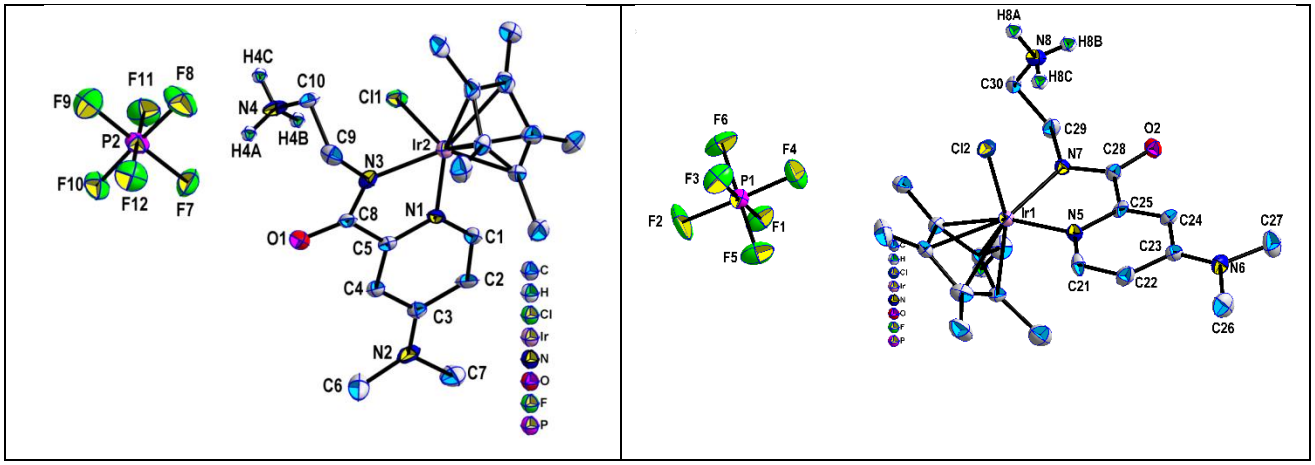

Figure S4: Crystal structure of unit-II of **Ir** complex. Selected bond lengths (Å) and angles (°) :C8─O1 1.272(12); C8─N3 1.340(12); C9─N3 1.446(11); C9─C10 1.518(13); C10─N4 1.492(13); Cl1─Ir2 2.428(2); Ir2─N1 2.051(8); Ir2─N3 2.084(8); N1─Ir2─Cl1 85.7(3); N1─ Ir2─N3 76.5(3); N3─Ir2─Cl1 84.6(2).	**Figure S5:** Crystal structure of unit-I of **Ir** complex. Selected bond lengths (Å) and angles (°) :C28─O2 1.261(11); C28─N7 1.342(12); C29─N7 1.458(12); C29─C30 1.535(14); C30─ N8 1.461(14); Cl2─Ir1 2.433(2); Ir1─N5 2.077(9); Ir1─N7 2.080(8); N5─Ir1─Cl2 86.5(2); N5─Ir1─N7 76.5(3); N7─Ir1─Cl2 87.2(2).

Table S1: Crystalographic data of Ir Complex **1**:

Parameters	**Ir**
empirical formula	$C_{41}H_{64}Cl_4F_{12}\ Ir_2N_8O_2P_2$
fw	530.75
crystal system	monoclinic
space group	$P2_1/n$
a (Å)	14.0034(11)
b (Å)	12.3704(9)
c (Å)	30.741(2)
α (deg)	90
β (deg)	94.759(3)
γ (deg)	90
V (Å^3)	5306.9(7)
Z	4
T (K)	120(2)
2θ (deg)	4.22-67.88
*D*calcd (g cm^{-3})	1.899
F (000)	2968
Index ranges	$-22 \le h \le 23$ $-21 \le k \le 21$ $-51 \le l \le 49$
R_{int}	0.0596
Goodness-of-fit on *F*2	1.665
$R_1^a/wR_2^b\ [I > 2\sigma(I)]$	0.1065 /0.2784
R_1^a /wR_2^b [for all F_o2]	0.1501 / 0.2938

1.3 Synthesis of the Support [Al-H]

Generation of the isolated silanol groups required treatment at high temperatures under vacuum (10^{-5} mbar). KCC-1 (2.0 gm) was introduced to a quartz reactor kept in a tubular furnace. The treatment started with dehydration by heating up to 130 °C for 3 h, followed by dehydroxylation at 700 °C, for 16 to 20 hours, with a heating gradient of 1 °C /min. After thermal treatment, titration with methyl lithium was performed using ether as a solvent. Quantification of the released methane indicates that the amount of silanol groups (≡Si-OH) is 1.8 mmol/g of

KCC-1_{700}. The reaction of KCC-1_{700} with DIBAL was carried out in a double Schlenk tube. KCC-1_{700} (0.5 g) was reacted with DIBAL (1.0 equiv., 1.0 M in hexane), followed by the addition of dry n-pentane (3.0 mL) to obtain white powder. The white powder was washed with dry pentane (three times) to eliminate unreacted DIBAL. The solid product was dried under vacuum (10^{-5} mbar) for 12 h. Furthermore, the later obtained solid was introduced in a glass reactor (275 mL) and heated up to 400 °C (8 °C/h) for 1 h under a dynamic vacuum (10^{-5} mbar) to afford [(≡Si-O-Si≡)(-Si-O-)$_2$Al-H], **[Al-H]**.

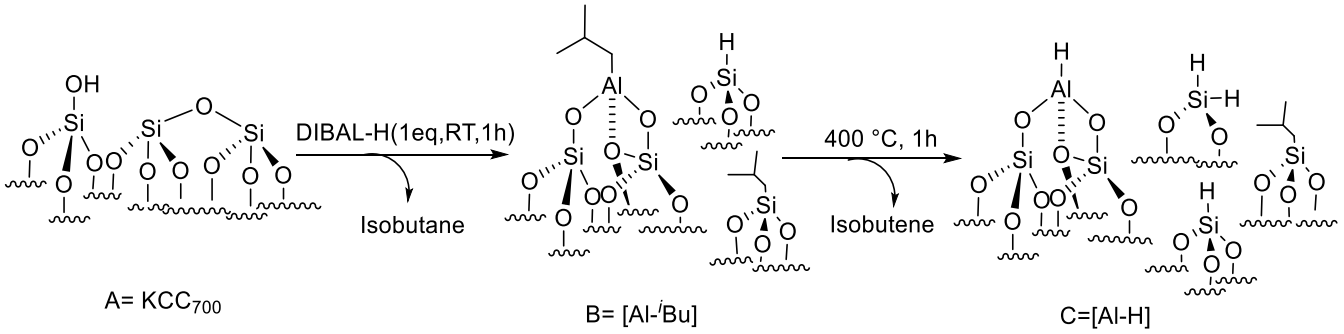

Scheme S2: Preparation of the **[Al-H]** support.

1.4 [Al-H] Support Characterization

The preparation of the support was monitored by FT-IR; Figure S6 displayed the spectrum of the dehydroxylated KCC-1_{700} (A, black line), with a sharp peak at 3743 cm^{-1} attributed to the isolated silanol groups (≡Si-OH), which drastically decreased after the reaction with the DIBAL-H to produce the [Al-^{i}Bu]. Moreover, different bands at 3000-2800 cm^{-1} and 1465-1365 cm^{-1} appeared, which are attributed, respectively, to ν[C-H] and δ[C-H] vibrations of the alkyl fragments, which were observed in both [Al-^{i}Bu] and the [Al-H]. Figure S6 shows the appearance of the new peaks at 2252-2170 cm^{-1}, characteristic of the [≡Si-H] and [=Si-H$_2$], respectively.

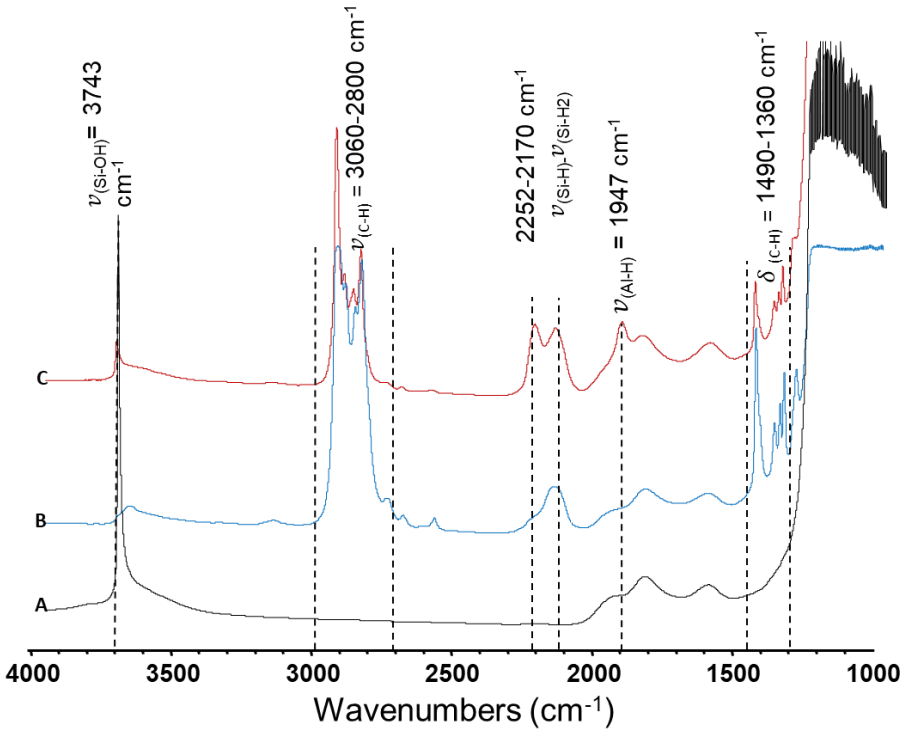

Figure S6. FT-IR spectrum of the A) KCC-1_{700} [(≡Si-O-Si≡)(≡Si-OH)], B) [(≡Si-O-Si≡)(-Si-O-)$_2$Al-^{i}Bu] [Al-^{i}Bu], C) the support [(≡Si-O-Si≡)(-Si-O-)$_2$Al-H] [Al-H]

1.5 Synthetic Procedure for Immobilization of 1 onto [Al-H]

In a double Schlenk flask, **[Al-H]** (500 mg, $n_{[Al]}$ = 0.65 mmol) was reacted at room temperature with complex **1** (61 mg, $n_{[1]}$ = 0.13 mmol) in dry CH_2Cl_2 (10 mL). After 4 h, the reaction was stopped, and the liquid phase was filtered into the second part of the double-Schlenk by inversing its position. Three washing and filtration cycles were performed, and the high vacuum line technique was used for 24 h to remove the remaining solvent. Solid product **2** was obtained and characterized using the following techniques and stored in a storage tube in the glove box.

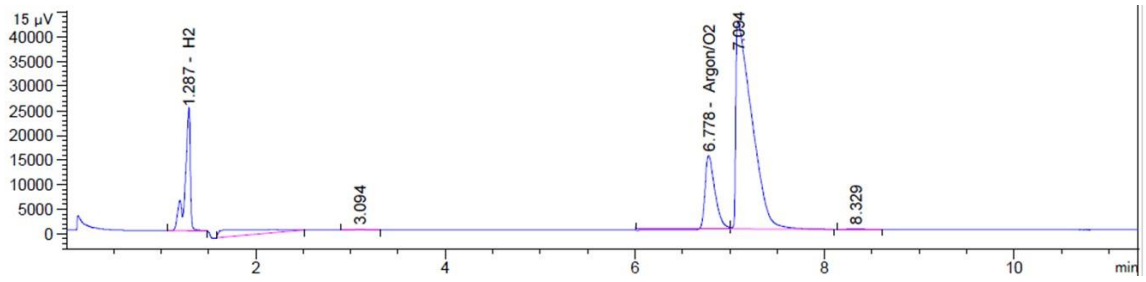

Figure 7. Gas analysis during immobilization reaction

1.6 Characterization of the Immobilized Complex 2

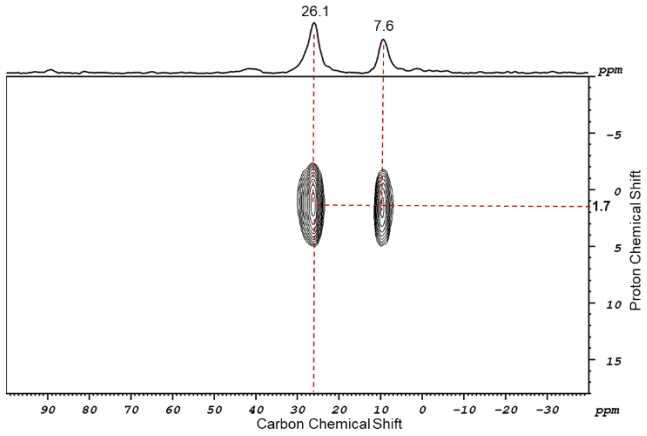

Figure S8. ^{1}H-^{13}C HETCOR solid-state NMR spectra of catalyst **2**

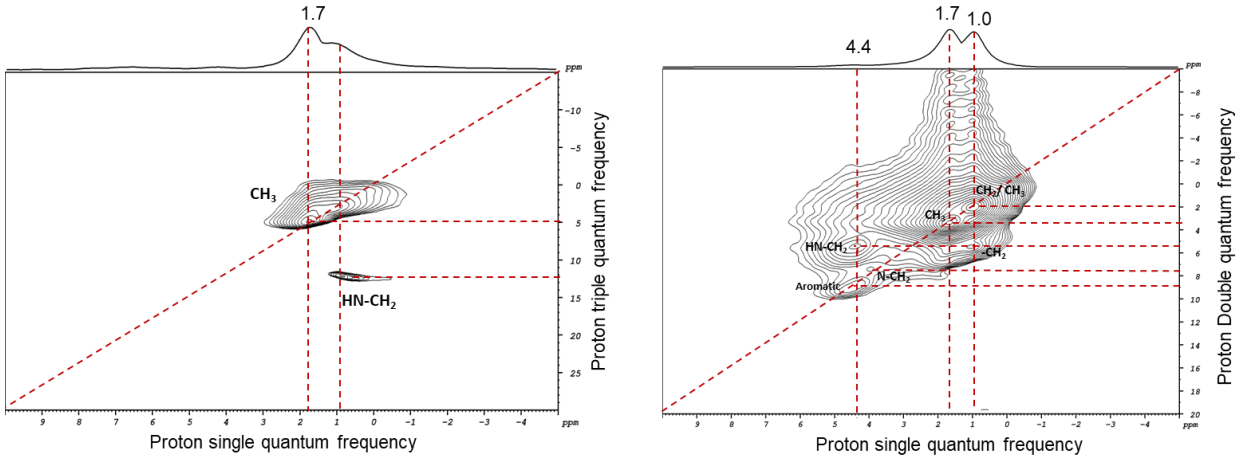

Figure S9. ^{1}H-^{1}H DQ solid-state NMR spectra of **2** (right), ^{1}H-^{1}H TQ solid-state NMR spectra of **2** (left).

In the ^{1}H-^{1}H DQ solid-state NMR spectra (Figure S9, right), the proton resonance assigned to alkyl groups CH_3/CH_2 at 1.0 ppm in the F2 shows a strong autocorrelation with the proton at 1.9 ppm in the F1, [1.9 ppm in F1: $\delta_H(CH) + \delta_H(CH) = 1.0 + 1.0$]. A strong autocorrelation at 1.7 ppm of methyl groups in the ω1 dimensions, [3.4 ppm in F1: $\delta_H(CH) + \delta_H(CH) = 1.7 + 1.7$]. The signal in the F2 at 4.4 ppm assigned aromatic protons showed autocorrelation at 8.7 ppm in the F1, [8.7 ppm in F1: $\delta_H(CH) + \delta_H(CH) = 4.4 + 4.4$]. The autocorrelation of CH_2-N moiety can be observed around 7.8 in the F2 [7.8 ppm in F1: $\delta_H(CH) + \delta_H(CH) = 4.4 + 4.4$]. Outside the diagonal, a

strong correlation at 5.4 ppm attributed to the protons near the CH_2-N-H group [5.4 ppm in F1: $\delta_H(NH) + \delta_H(CH) = 4.4+1.0$]. The ^1H TQ solid-state NMR spectra of **2** were also recorded (Figure S9, left), it shows an autocorrelation at 5 ppm in F1 corresponding to the methyl groups. Outside the diagonal, a correlation of 12.3 ppm in the F1 was attributed to the CH_2-N-H group.

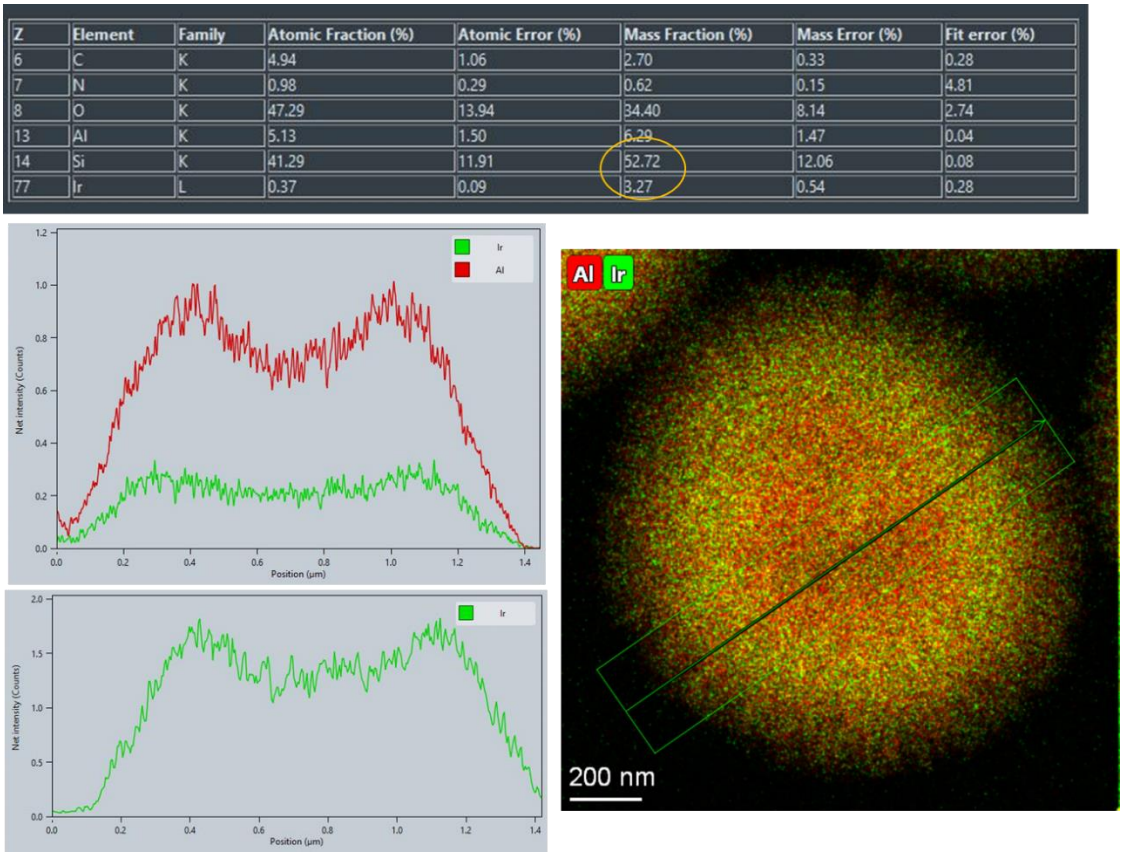

Z	Element	Family	Atomic Fraction (%)	Atomic Error (%)	Mass Fraction (%)	Mass Error (%)	Fit error (%)
6	C	K	4.94	1.06	2.70	0.33	0.28
7	N	K	0.98	0.29	0.62	0.15	4.81
8	O	K	47.29	13.94	34.40	8.14	2.74
13	Al	K	5.13	1.50	6.29	1.47	0.04
14	Si	K	41.29	11.91	52.72	12.06	0.08
77	Ir	L	0.37	0.09	3.27	0.54	0.28

Figure S10. TEM analysis of catalysts **2**

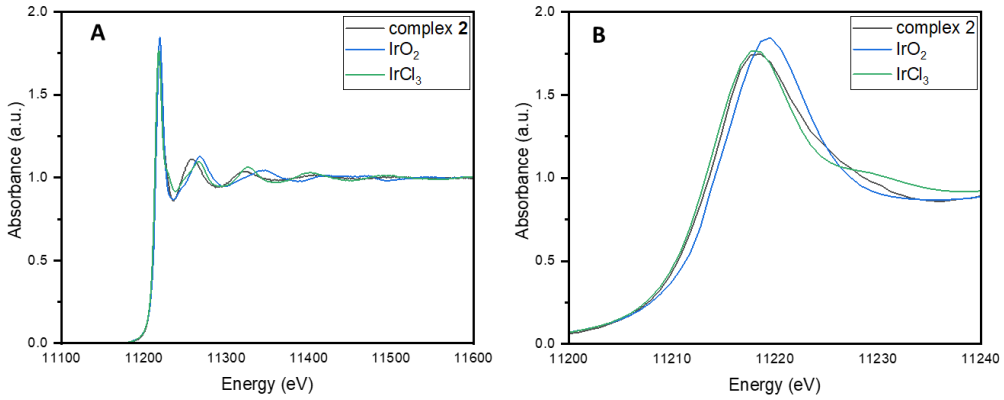

Figure S11. A) The normalized XANES spectra of **2**, B) zoomed-in view

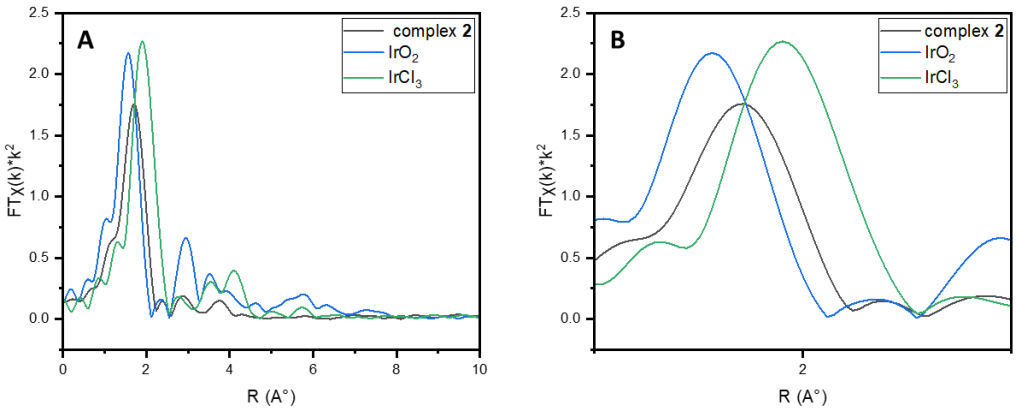

Figure S12. A) Fourier transformation magnitudes of EXAFS spectra of **2.** B) Zoom in view.

Table S2. EXAFS fitting results of complex **2**

path	CN	σ^2	ΔE_0	R	R-factor
Ir-N	4.5(0.7)	0.0077(0.0014)	7.20(1.41)	2.10(0.02)	0.005
Ir-Cl	1.8(0.9)	0.0077(0.0014)	7.20(1.41)	2.32(0.02)	

2. Catalytic test: FA Dehydrogenation

2.1 General Procedure for the Dehydrogenation of FA Catalyzed by 1: The formic acid dehydrogenation experiment was carried out in a two-necked round flask equipped with a reflux condenser and a magnetic stirrer at an appropriate temperature. The catalyst stock solution (FA/cat.**1**, 30 mmol/ 2.0 μmol) was prepared freshly before use. The catalyst stock solution was injected through a septum into a flask containing NaO_2CH (30 mmol,1 g). The evolution of the generated gas was observed and monitored simultaneously using an ADM G6691A flowmeter. The data was collected every 2 seconds on the computer by lab view.

2.2 General Procedure for the Continuous Flow Catalytic Dehydrogenation of FA Catalyzed by 1: The formic acid dehydrogenation experiment was carried out in a two-necked round flask equipped with a reflux condenser and a magnetic stirrer at an appropriate temperature. The catalyst stock solution (FA/cat. **1**, 30 mmol/ 2.0 μmol) was prepared freshly before use. The catalyst stock solution was injected through a septum into a flask containing NaO_2CH (30 mmol,1 g). Then, formic acid was added via a syringe pump at a constant rate, where the

rate of consumption and the rate of addition remained the same. The evolution of the generated gas was observed and monitored using an ADM G6691A flowmeter simultaneously. The data was collected every 2 seconds to the computer by lab view.

2.3 General Procedure for Dehydrogenation of FA Catalyzed by 2: The formic acid dehydrogenation experiment was performed in a two-necked round flask equipped with a reflux condenser and a magnetic stirrer at 90 °C. The Catalyst **2** (2.0 μmol, 10 mg) and NaO_2CH (30 mmol, 1 g) were weighed inside the glovebox and transferred into the two-necked round flask and Formic acid (30 mmol, 1.2 mL) was added via syringe. The evolution of the generated gas was observed and monitored using an ADM G6691A flowmeter simultaneously. The data was collected every 2 seconds to the computer by lab view.

2.4 General Procedure for the Continuous Flow Catalytic Dehydrogenation of FA Catalyzed by 2: The formic acid dehydrogenation experiment was carried out in a two-necked round flask equipped with a reflux condenser and a magnetic stirrer at an appropriate temperature. The catalyst **2** (2 μmol, 10 mg) and NaO_2CH (30 mmol, 1g) were weighed inside the glovebox and transferred into the two-necked round flask. Formic acid was added via a syringe pump at a constant rate, where the rate of consumption and the rate of addition remained the same. The evolution of the generated gas was observed and monitored using an ADM G6691A flowmeter simultaneously. The data was collected every 2 seconds to the computer by lab view.

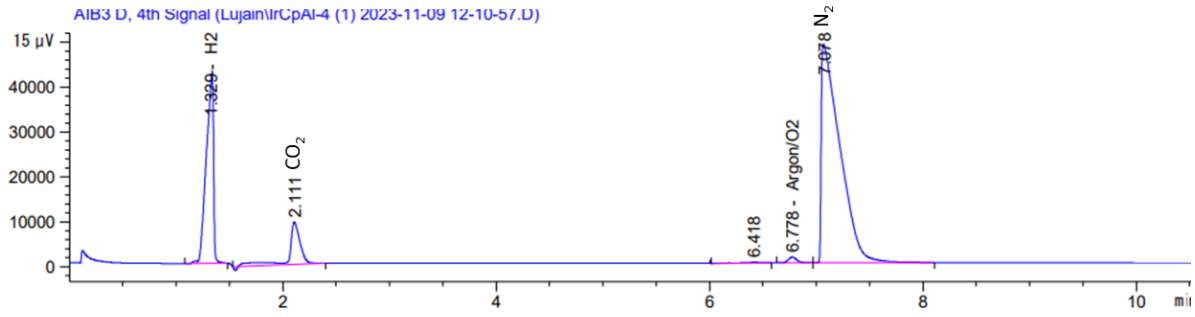

Figure S13. Gas-phase analysis of FA dehydrogenation by catalyst **2**

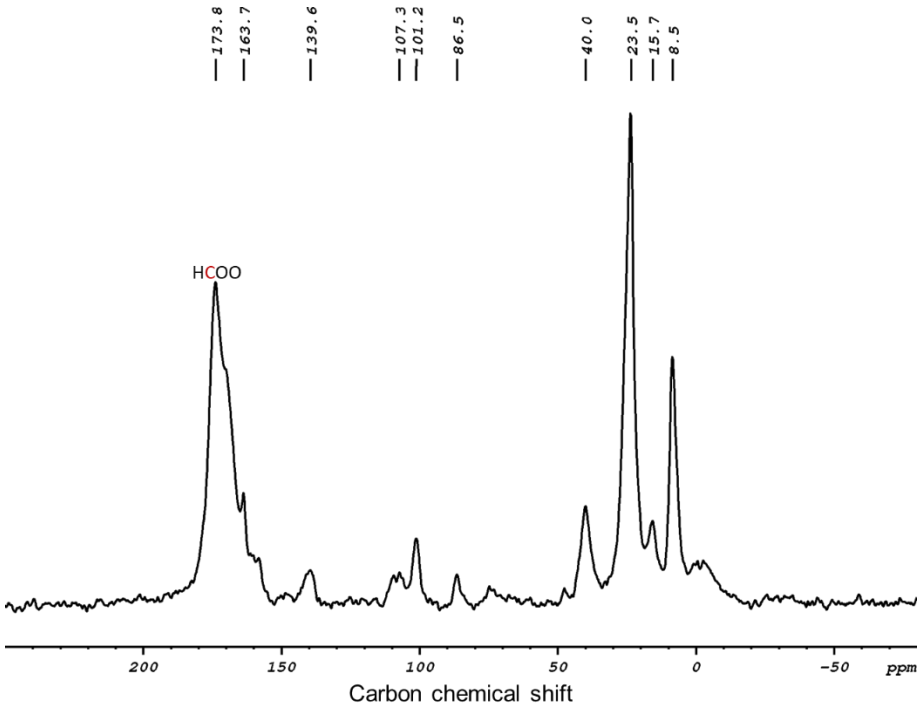

Figure S14. ^{13}C/CP MAS solid-state NMR spectrum of the intermediate 2a

Table S3. Bases screening in FA dehydrogenation by catalyst **2**[a]

Entry	Conditions	TOF	Yield
1	NaO_2CH	40,000 h^{-1}	88%
2	KO_2CH	71,770 h^{-1}	47%
3	KOH	26,000 h^{-1}	19%
4	NaOH	62,200 h^{-1}	53%
5	Na_2CO	42,890 h^{-1}	51%

[a]General conditions: FA (1.2 ml, 30 mmol), FA/Base =1:1, Catalyst 2 (10 mg, 2 μmol), temperature (90 °C). The maximum TOF was estimated based on the H_2 production in the first 10 min.

Table S4. FA concentration study in Dehydrogenation by catalyst **2**[a]

Entry	Conditions	TOF	Yield
1	FA 99%	37,000 h^{-1}	90 %
2	FA 95%	44,000 h^{-1}	87 %
3	FA 91%	51,000 h^{-1}	98%

[a]General conditions: FA (1.2 ml, 30 mmol), Catalyst **2** (10 mg, 2 µmol) temperature (90 °C). The maximum TOF was estimated based on the H_2 production in the first 10 min.

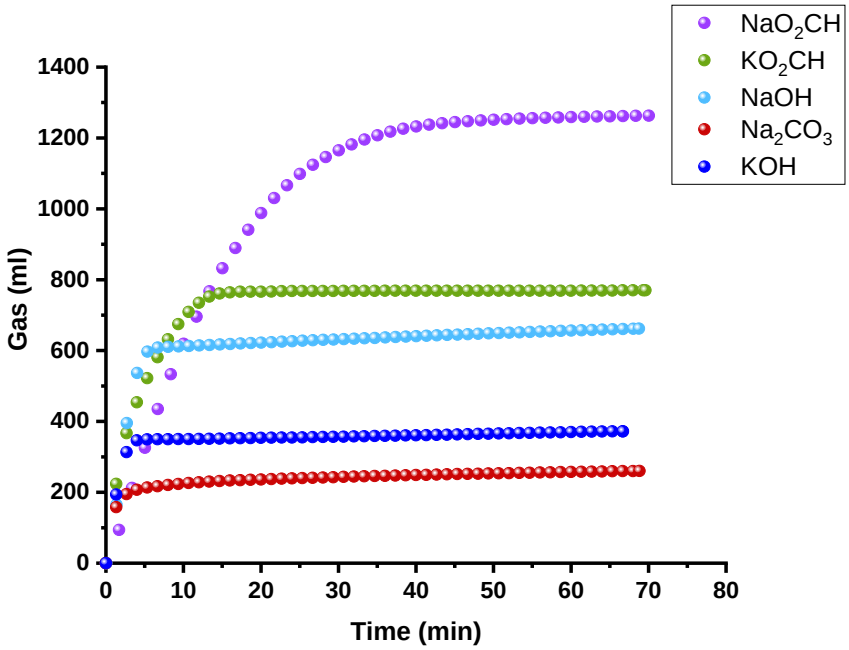

Figure S15. Graphical plot of the dehydrogenation reaction by catalyst **2** in Bases screening

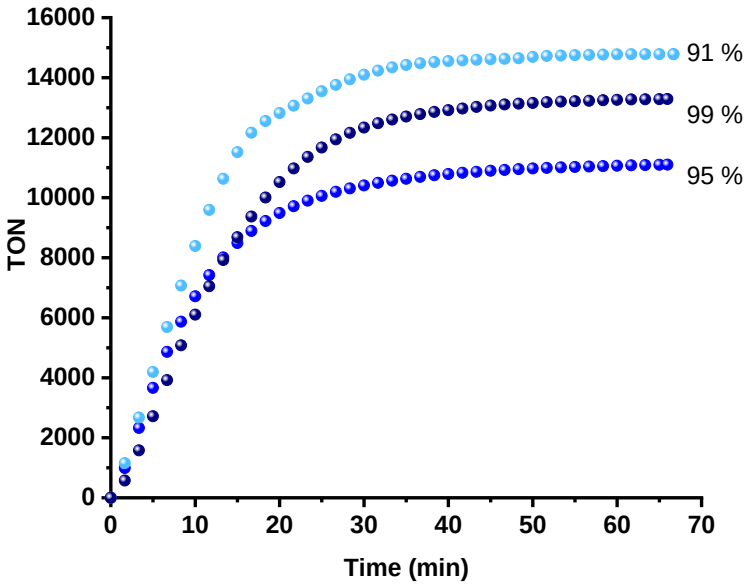

Figure S16. Graphical plot of the dehydrogenation reaction by catalyst **2** when different concentration of FA was used.

After the long-term reaction, under the optimized reaction conditions, the reaction mixture was filtered. The liquid phase, which contained the leached catalyst, was dried first by Rotavap to remove the residual FA and water. After that, it was dissolved in d-chloroform and analyzed by NMR analysis.

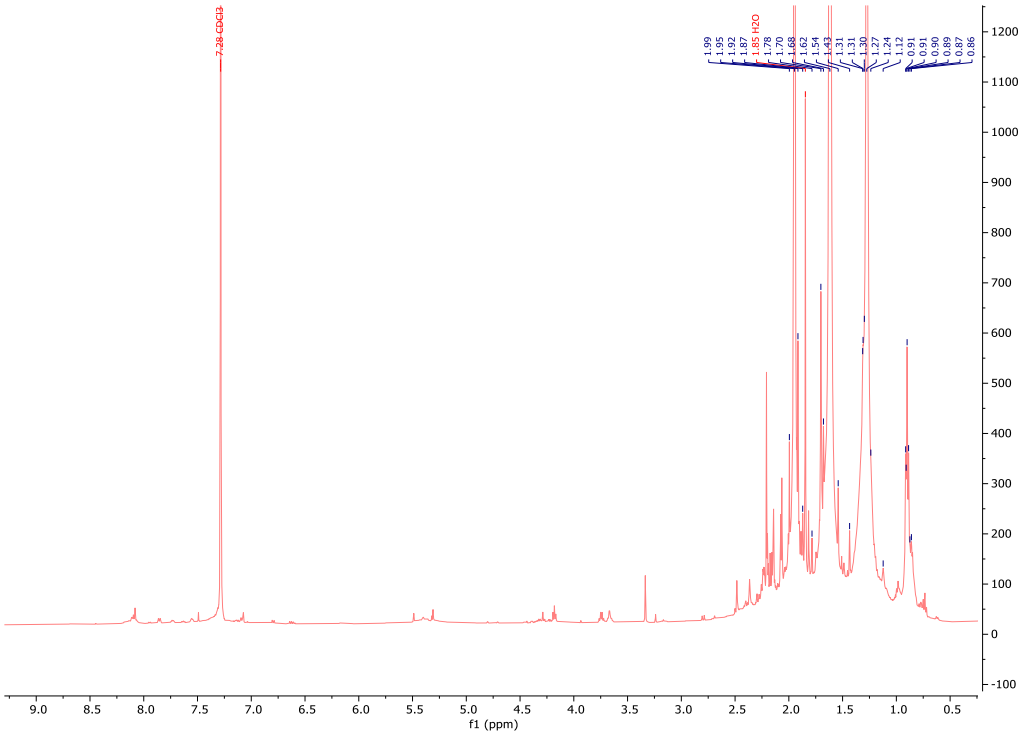

Figure S17. ^{1}H NMR spectrum of the leached catalyst after the reaction

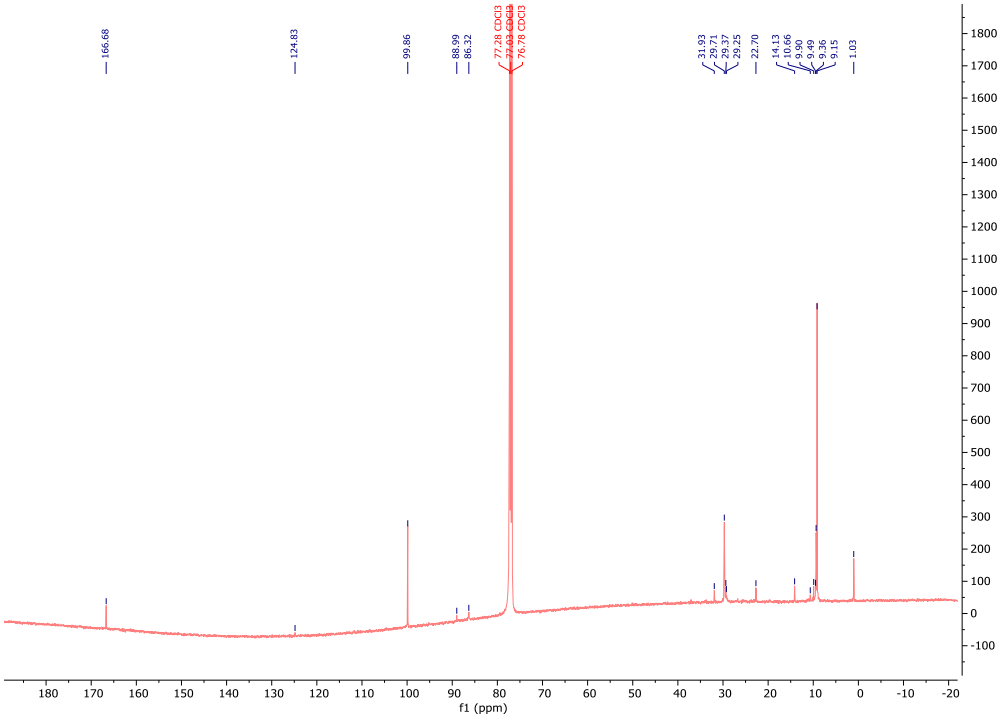

Figure S18. ^{13}C NMR spectrum of the leached catalyst after the reaction

3. TON and TOF Calculations

TON and TOF of formic acid dehydrogenation were calculated using the sum of H_2 and CO_2 volumes considered to be equal to the total volume of gas collected. Total volume was calculated as the product between the number of moles and the molar volume of the species.

$$\mathrm{V}_{H_2} + \mathrm{V}_{CO_2} = \mathrm{V}$$

$$\mathrm{n}_{H_2}\mathrm{V}_{m,H_2} + \mathrm{n}_{CO_2}\mathrm{V}_{m,CO_2} = \mathrm{V}$$

$$n(\mathrm{V}_{m,H_2} + \mathrm{V}_{m,CO_2}) = \mathrm{V}$$

$$n = \frac{\mathrm{V}}{(\mathrm{V}_{m,H_2} + \mathrm{V}_{m,CO_2})}$$

$TON = \frac{\mathrm{n}}{n_{cat}}$ where n_{cat} is the number of moles of the catalyst.

$TOF = \frac{\mathrm{TON}}{T}$ where the T is time in hours (h)

The yield was calculated based on the following equation:

$$Yield = \frac{V}{\mathrm{V}_{theoritical}} \times 100$$

$$\mathrm{V}_{theoritical} = n_{Formic\ acid}\left(\mathrm{V}_{m,H_2} + \mathrm{V}_{m,CO_2}\right)$$

We used 30 mmol of formic acid in our case, and the molar volume values are explained below. Therefore, the theoretical volume was calculated as follows:

$$\mathrm{V}_{theoritical} = 0.030mol\ (24.48\ L\ mol^{-1} + 24.36\ L\ mol^{-1}) = 1.1652\ L \text{ (or 1165 mL)}$$

To calculate the molar volume for both H_2 and CO_2, the following equations were used:

$$\mathrm{V}_{m,H_2} = \frac{RT}{p} + b - \frac{a}{RT} = 24.48\ L\ mol^{-1}$$

Where:

$R = 8.31447\ m^3 Pa\ mol^{-1} K^{-1}$

$T = 298.15\ K$

$p = \ 101325\ Pa$

$b = 26.7\ \times 10^{-6}\ m^3 mol^{-1}$

$a = 2.49\ \times 10^{-10}\ Pa\ m^3 mol^{-2}$

$\mathrm{V}_{m,CO_2} = \frac{RT}{p} + b - \frac{a}{RT} = 24.36\ L\ mol^{-1}$

Where:

$R = 8.31447\ m^3 Pa\ mol^{-1} K^{-1}$

$T = 298.15\ K$

$p = \ 101325\ Pa$

$b = 42.7\ \times 10^{-6}\ m^3 mol^{-1}$

$a = 36.5\ \times 10^{-10}\ Pa\ m^3 mol^{-2}$

$\mathrm{n}_{H_2} = \mathrm{n}_{CO_2} = \mathrm{n}$

4. DFT Methods

The Vienna ab initio Simulation Package (VASP) was used to perform periodic, spin-polarized plane-wave density functional theory (DFT) calculations.[1, 2] Core electrons were represented via projector augmented-wave (PAW) pseudopotentials,[3, 4] while valence electrons were expanded in terms of a plane-wave basis with an energetic cutoff of 600 eV. Exchange and correlation effects were treated with the Perdew-Burke-Ernzerhof (PBE) functional,[5] while dispersion effects were accounted for using Grimme's DFT-D3 method.[6] The Brillouin zone was sampled at the Γ-point only. Fermi surfaces were treated with Gaussian smearing with a smearing width of 0.05 eV to help accelerate electronic convergence. The final energies were then obtained by extrapolating to 0 K.

The atomistic model for the **[Al-H]** support was obtained from our previous works.[7, 8] The model consists of a 252-atom amorphous silica slab with a surface silanol group (≡Si-OH) density of 1.69 nm^{-2}. The initial structure was obtained from the reference [9]; the cell and ionic positions were reoptimized for consistency with our computational setup. At least 12 Å of vacuum in the *z*-direction was maintained between the periodic images of the surface to prevent spurious interactions. All atoms in the system were allowed to relax; ionic relaxation was stopped when the Hellmann-Feynman forces on all atoms were less than 0.02 eV $Å^{-1}$.

Transition states were located using the climbing-image nudged elastic band (CI-NEB) method as implemented in VTST.[10] Each band comprised of seven images, excluding the initial and final state images, and was optimized until the forces on all atoms on all images were less than 0.02 eV $Å^{-1}$. Located transition states were confirmed by the presence of a single imaginary mode in subsequent vibrational analyses.

All energies presented in potential energy diagrams are Gibbs free energies referenced to HCOOH(g) and the clean activated catalyst **1** or **2**. The Gibbs free energy of an adsorbate on the catalyst, G_{ads}, is thus calculated as:

$$G_{\mathrm{ads}} = G_{\mathrm{tot,ads}} - G_{\mathrm{tot,clean}} - G_{\mathrm{tot,HCOOH(g)}}\ , \qquad (1)$$

where $G_{\mathrm{tot,ads}}$ is the total Gibbs free energy of the adsorbate+surface system, $G_{\mathrm{tot,clean}}$ is the total Gibbs free energy of the clean catalyst and $G_{\mathrm{tot,HCOOH(g)}}$ is the total Gibbs free energy of HCOOH in the gas-phase.

Gibbs free energies were obtained by correcting the total electronic DFT energies with zero-point energy (ZPE) and finite-temperature enthalpic and entropic contributions calculated from the normal mode harmonic vibrational frequencies. To reduce spurious contributions due to small vibrational frequencies, we used the quasi-rigid-rotor-harmonic-oscillator (quasi-RRHO) approximation [11] with a frequency cutoff of 35 cm^{-1}. The normal mode harmonic vibrational frequencies were obtained by building up the Hessian via a finite-differences approach with a step size of 0.007 Å and subsequent diagonalization of the mass-weighed Hessian. To reduce the computational cost of the frequency calculations, we relaxed only the adsorbates, water molecules, the Ir metal center and its ligands, the Al atom, and the two oxygen atoms bonded to Al, while fixing all other atoms in the system.

Machine Learning Accelerated Simulated Annealing Molecular Dynamics (SA-MD) Simulations

To locate stable ground state structures of catalysts **1** and **2**, SA-MD simulations were performed in the Atomic Simulation Environment (ASE).[12] The initial temperature was set to 300 K and ramped down to 10 K in the span of 300000 steps with a timestep of 1 fs each. The simulations sampled the NVT ensemble with a Nosé-Hoover thermostat.[13, 14] For each catalyst, 8 SA-MD replicas were performed to rigorously sample the configurational space. To accelerate these computationally costly simulations, equivariant graph neural network (GNN)-based

machine learning potentials of the MACE architecture[15] were trained using first-principles DFT calculations obtained on-the-fly by sampling of uncertain configurations in the SA-MD simulations. The uncertainty of a configuration was quantified by using an ensemble of two MACE models and summing up the standard deviations of the predicted energies and forces. Configurations were selected for sampling when the uncertainty was greater than 0.2. The final MACE models were trained on 162 (120) configurations and showed energy and force root mean square errors (RMSEs) of 0.036 (0.051) eV and 0.017 (0.019) eV/Å, for catalyst **1 (2)**.

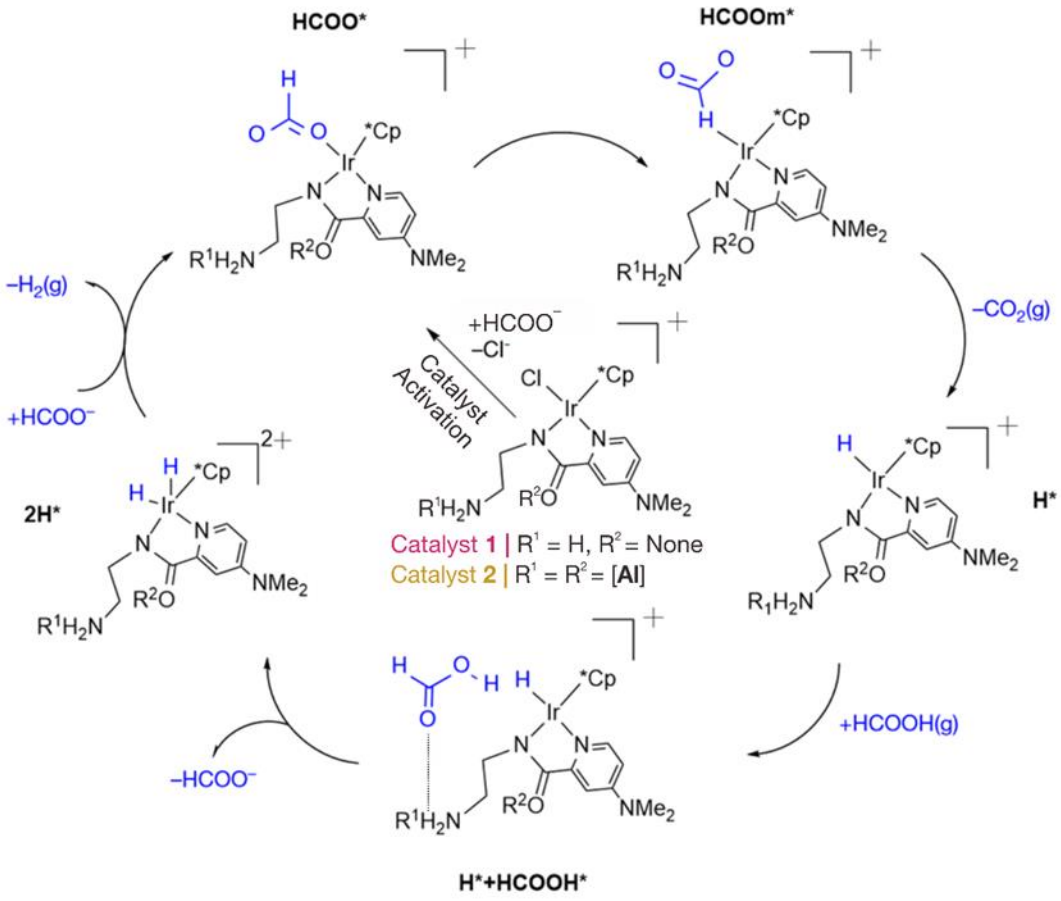

Figure S19. FA decomposition cycle over catalysts **1** and **2** with FA. Catalysts **1** and **2** are first activated via ligand exchange of Cl^- with $HCOO^-$, forming the HCOO* state. The activated catalysts can then undergo repeated catalytic cycles decomposing FA into CO_2(g) and H_2(g). Reactants, intermediates, and products are highlighted in blue font for clarity.

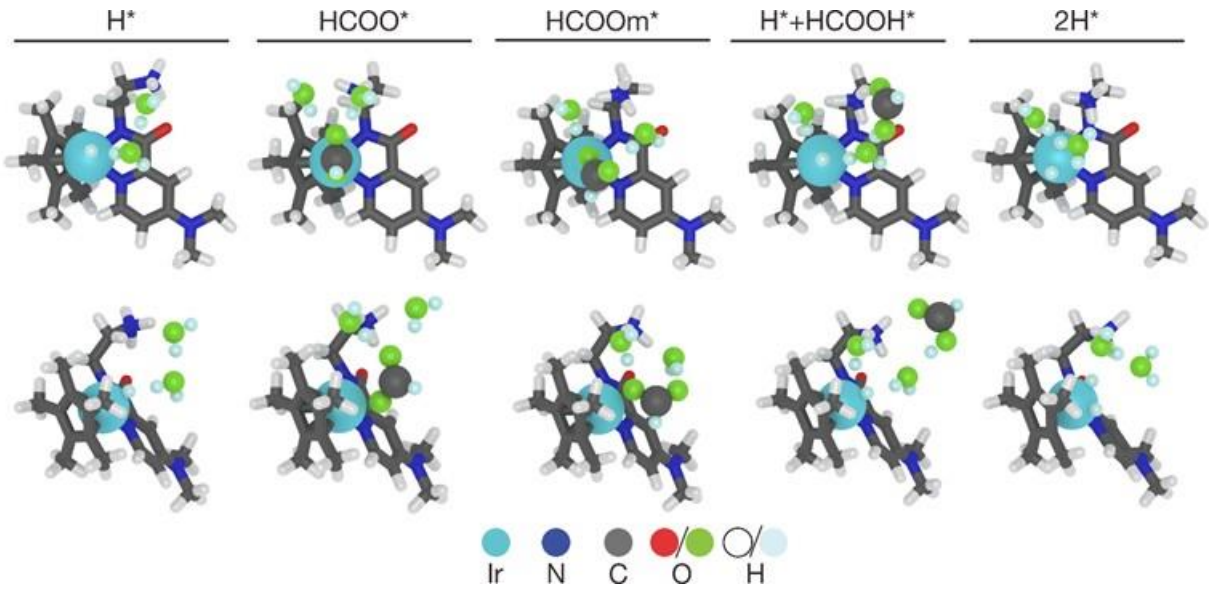

Figure S20. Atomic illustrations of the intermediates involved in FA decomposition over the activated homogeneous catalyst **1**. For clarity, the ligands of the Ir center are shown as sticks. First row: side view, second row: top view. Color code: H – white, C – grey, Ir – cyan, N – blue, O of H_2O and adsorbates – green, H of H_2O and adsorbates – light blue.

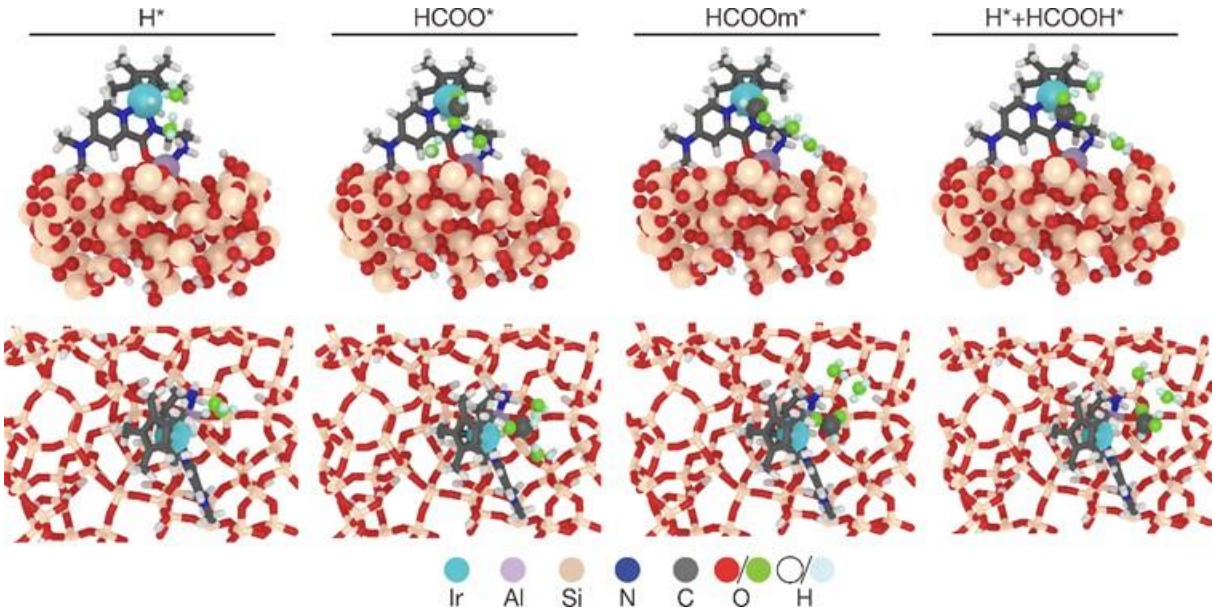

Figure S21. Atomic illustrations of the intermediates involved in FA decomposition over the activated grafted catalyst **2**. For clarity, the ligands of the Ir center are shown as sticks. First row: side view, second row: top view. The support is also shown as sticks in the top view for further clarity. Color code: Si – beige, O – red, H – white, C – grey, Al – purple, Ir – cyan, N – blue, O of H_2O and adsorbates – green, H of H_2O and adsorbates – light blue.

5. Characterization Tools and Specifications

Liquid-State Nuclear Magnetic Resonance Spectroscopy: NMR spectra were recorded on Bruker Advance 400 in deuterated solvents. ^{1}H NMR chemical shifts were referenced to the residual hydrogen signals of the deuterated solvents, and the ^{13}C NMR chemical shifts were referenced to the ^{13}C signals of the deuterated solvents. Data are reported as follows: chemical shift, multiplicity (s = singlet, d = doublet, t = triplet, q = quartet, p = pentet, s = sextet, h = heptet, m =multiplet, br = broad).

Elemental Analysis: The analytical technique Inductively Coupled Plasma Optical Emission Spectrometry (ICP-OES) is used to determine the metal loading in percentage for each complex while the CHN analyzer determines the carbon and the nitrogen fractions. Since the Al-modified [Al-H] support contains carbon 6.7 wt.% (5.6 $mmol.g^{-1}$), the total amount of carbon after grafting was 12.03 wt. % (10.1 $mmol.g^{-1}$); this value includes the amount of carbon remaining on the support as [≡Si-^{i}Bu]. To find the C/Ir ratio, which corresponds to the ligands, we subtract the total amount of carbon by the amount of carbon present on the support to determine the amount of carbon resulting from the grafting of the organometallic complex.

$$C_{(\text{carbon of ImbIr})} = C_{(\text{total carbon}|)} - C_{(\text{carbon from } \equiv\text{Si-isobutyl on modified support})}$$

$$= 10.1 - 5.6 = 4.5\ mmol.g^{-1}$$

Infrared analysis: Spectra were collected on a Nicolet 6700 FT-IR spectrometer equipped with a cell under a controlled atmosphere. Typically, 32 scans were accumulated for each spectrum (resolution 6 cm^{-1}). The FT-IR of **1** pre-grafting complex, was taken after granting **1** with dry KBr, the spectra show all the characteristic peaks of **1**.

X-ray Adsorption spectroscopy (XAS): The X-ray absorption fine structure (XAFS) spectra at Ir L-edge were performed at the XAFCA beamline of Singapore Synchrotron Light Source (SSLS) operated at 0.7 GeV with a current of 150 mA. The XAFS data were recorded under transmission mode with ionization chamber detectors placed upstream and downstream of the sample. The energy was calibrated according to the absorption edge of pure Ir powder. Athena and Artemis codes were used to extract the data and fit the profiles. For the X-ray absorption near edge structure (XANES) part, the experimental absorption coefficients as a function of energies μ(E) were

processed by background subtraction and normalization procedures and reported as “normalized absorption”. For the extended X-ray absorption fine structure (EXAFS) part, the Fourier transformed (FT) data were analyzed by applying first-shell approximate model for Ir-O and Ir-Cl contribution. The experimental data on Ir powder with fixing the coordination number (CN) of Ir-Ir for further analysis of the measured samples. The parameters describing the electronic properties (e.g., correction to the photoelectron energy origin, ΔE0) and local structure environment including CN, bond distance (R) and Debye-Waller (D.W.) factor around the absorbing atoms were allowed to vary during the fit process.

X-ray Diffraction spectroscopy (XRD): X-ray quality crystals were immersed in cryo-oil, mounted in a Nylon loop, and measured at 120 K. Intensity data were collected using a Bruker D8 Venture SMART CCD diffractometer with graphite monochromated Mo−Kα (λ = 0.71073 Å) radiation. Cell parameters were retrieved using Bruker SMART software[2] and refined using Bruker SAINT[2] on all the observed reflections. Data were corrected for absorption effects using the multi-scan method (SADABS). Structures were solved by direct methods by using the SHELXS-2016 package and refined with SHELXL-2016.

All other hydrogen atoms in the compound were inserted on geometrical calculated positions with fixed thermal parameters. All the hydrogen atoms, either located or inserted, were refined isotropically, while all the nonhydrogen atoms were refined anisotropically. The final least-squares refinements (R_1) based on $I > 2\sigma(I)$ converged to 0.1065 for Ir complex.

Transmission electron microscopy (TEM): TEM analysis is performed on a Titan Themis Z electron microscope (Thermo Fisher Scientific), equipped with a Super-X energy dispersive x-ray spectrometer system, and a GIF Continuum K3 electron energy loss spectrometer (Gatan Inc.)

Gas-phase analysis: The gas analysis was carried out using the Agilent Technologies 7890B series gas chromatograph has been custom configured by Wasson-ECE Instrumentation per quotation authorization number 020117-JT1 for the analysis of extended refinery gas and liquid analysis and analysis of oxygenates. Components analyzed on TCD include hydrogen, carbon dioxide, ethylene, ethane, acetylene, hydrogen sulfide, oxygen/argon composite, nitrogen, methane, and carbon monoxide. The gas obtained during the reaction was collected and subjected to qualitative analysis. The observed chromatograms suggested the generation of H_2 and CO_2 without detecting any trace of CO which consequently demonstrated the selectivity as no side reaction was occurring.

Solid-State Nuclear Magnetic Resonance Spectroscopy: One-dimensional ^{1}H MAS and ^{13}C CP/MAS solid-state NMR: Spectra were recorded on a Bruker AANCE III spectrometer operating at 600 MHz resonance frequencies for ^{1}H employing a conventional double-resonance 3.2 mm probe. In all cases, the samples were packed into zirconium rotors under an inert atmosphere inside a glovebox. Dry nitrogen gas was used for sample spinning to

prevent the degradation of the samples. NMR chemical shifts are reported with respect to the external references TMS and adamantane. For ^{13}C CP/MAS NMR experiments, the following parameters were used: a 90° proton pulse length of 2.9 μs, a contact time of 5 ms, with high-power proton decoupling with a recycle delay of 5 s, and the number of scans was 18 000.

^{1}H-^{1}H multiple-quantum NMR spectroscopy: Two-dimensional double-quantum and triple-quantum experiments were recorded on a Bruker Avance III spectrometer operating at 600 MHz with a conventional double resonance 3.2 mm CP/MAS probe, according to the following general scheme: excitation of DQ coherences, t1 evolution, z-filter, and detection. The spectra were recorded in a rotor-synchronized fashion in t1 by setting the t1 increment equal to one rotor period. One cycle of the standard back-to-back recoupling sequences was used for the excitation and reconversion period. Quadrature detection in w1 was achieved using the states-TPPI method. A MAS frequency of 20 kHz was used. The 90° proton pulse length was 2.5 μs, while a recycle delay of 5 s was used. A total of 128 t1 increments with 32 or 128 scans each increment was recorded. The DQ frequency in the ω1 dimension corresponds to the sum of two single-quantum (SQ) frequencies of the two coupled protons and correlates to the ω2 dimension with the two corresponding proton resonances. The TQ frequency in the ω1 dimension corresponds to the sum of the three SQ frequencies of the three coupled protons and correlates to the ω2 dimension with the three individual proton resonances. Conversely, groups of less than three equivalent spins will not give rise to diagonal signals in this spectrum.

6. References

1. G. Kresse and J. Furthmüller, Efficiency of ab-initio total energy calculations for metals and semiconductors using a plane-wave basis set, *Comput. Mater. Sci.*, 1996, **6**, 15-50.

2. G. Kresse and J. Furthmüller, Efficient iterative schemes for ab initio total-energy calculations using a plane-wave basis set, *Phys. Rev. B.*, 1996, **54**, 11169-11186.

3. P. E. Blöchl, Projector augmented-wave method, *Phys. Rev. B.*, 1994, **50**, 17953-17979.

4. G. Kresse and D. Joubert, From ultrasoft pseudopotentials to the projector augmented-wave method, *Phys. Rev. B.*, 1999, **59**, 1758-1775.

5. J. P. Perdew, K. Burke and M. Ernzerhof, Generalized Gradient Approximation Made Simple, *Phys. Rev. Lett.*, 1996, **77**, 3865-3868.

6. S. Grimme, J. Antony, S. Ehrlich and H. Krieg, A consistent and accurate ab initio parametrization of density functional dispersion correction (DFT-D) for the 94 elements H-Pu, *J. Chem. Phys.*, 2010, **132**, 154104.

7. L. Yaacoub, I. Dutta, B. Werghi, B. W. J. Chen, J. Zhang, E. A. Hamad, E. P. Ling Ang, E. Pump, A. B. Sedjerari, K.-W. Huang and J.-M. Basset, Formic Acid Dehydrogenation via an Active Ruthenium Pincer Catalyst Immobilized on Tetra-Coordinated Aluminum Hydride Species Supported on Fibrous Silica Nanospheres, *ACS Catal.*, 2022, **12**, 14408-14417.

8. L. Alrais, S. S. Gholap, I. Dutta, E. Abou-Hamad, B. W. J. Chen, J. Zhang, M. N. Hedhili, J.-M. Basset and K.-W. Huang, Highly efficient immobilized PN^3P-pincer iridium catalyst for dehydrogenation of neat formic acid, *Appl. Catal. B* . 2024, **342**, 123439.

9. L. Li, C. S. Ewing, M. Abdelgaid, S. Banerjee, R. B. Garza, R. Hacku, N. D. Hess, S. Hong, M. Islamov, L. L. Luciani, S. Papadopoulos, C. Parker, R. A. Patel, R. Pawar, M. H. Poklar, M. Salem, F. Shabnam, P. B. Shukla, S. K. Vena, H. Wang, R. Wang, X. Wei, F. Yang and J. K. Johnson, Binding of CO and O on Low-Symmetry Pt Clusters Supported on Amorphous Silica, *J. Phys. Chem. C*, 2021, **125**, 13780-13787.

10. G. Henkelman, B. P. Uberuaga and H. Jónsson, A climbing image nudged elastic band method for finding saddle points and minimum energy paths, *J. Chem. Phys.*, 2000, **113**, 9901-9904.

11. S. Grimme, Supramolecular Binding Thermodynamics by Dispersion-Corrected Density Functional Theory, *Eur. J. Chem.*, 2012, **18**, 9955-9964.

12. A. Hjorth Larsen, J. Jørgen Mortensen, J. Blomqvist, I. E. Castelli, R. Christensen, M. Dułak, J. Friis, M. N. Groves, B. Hammer, C. Hargus, E. D. Hermes, P. C. Jennings, P. Bjerre Jensen, J. Kermode, J. R. Kitchin, E. Leonhard Kolsbjerg, J. Kubal, K. Kaasbjerg, S. Lysgaard, J. Bergmann Maronsson, T. Maxson, T. Olsen, L. Pastewka, A. Peterson, C. Rostgaard, J. Schiøtz, O. Schütt, M. Strange, K. S. Thygesen, T. Vegge, L. Vilhelmsen, M. Walter, Z. Zeng and K. W. Jacobsen, The atomic simulation environment—a Python library for working with atoms, *J. Phys.: Condens. Matter*, 2017, **29**, 273002.

13. W. G. Hoover, Canonical dynamics: Equilibrium phase-space distributions, *Physical Review A*, 1985, **31**, 1695-1697.

14. S. Nosé, A unified formulation of the constant temperature molecular dynamics methods, *J. Chem. Phys.*, 1984, **81**, 511-519.

15. I. Batatia, D. a. P. e. Kov'acs, G. N. C. Simm, C. Ortner and G. Csányi, MACE: Higher Order Equivariant Message Passing Neural Networks for Fast and Accurate Force Fields, *ArXiv*, 2022, **abs/2206.07697**.